Electronic Supplementary Material (ESI) for Chemical Science.
This journal is © The Royal Society of Chemistry 2019

Electronic Supplementary Information (ESI) for

"Disrupt and Induce" Intermolecular Interactions to Rationally Design Organic Semiconductor Crystals: from Herringbone to Rubrene-like Pitched π-Stack

Chengyuan Wang,*[a] Daisuke Hashizume,[b] Masahiro Nakano,[a] Takuya Ogaki,[a] Hiroyuki Takenaka,[c] Kohsuke Kawabata,[c] Kazuo Takimiya*[ac]

[a.] Emergent Molecular Function Research Team, RIKEN Center for Emergent Matter Science (CEMS), 2-1 Hirosawa, Wako, Saitama 351-0198, Japan.
E-mail: chengyuan.wang@riken.jp; takimiya@riken.jp

[b.] Materials Characterization Support Team, RIKEN Center for Emergent Matter Science (CEMS), 2-1 Hirosawa, Wako, Saitama 351-0198, Japan

[c.] Department of Chemistry, Graduate School of Science, Tohoku University, 6-3 Aoba, Aramaki, Aoba-ku, Sendai, Miyagi 980-8578, Japan

Table of Contents

Experimental Procedures ····· 3

Synthesis of compounds ····· 3

Methods and instruments ····· 3

Results and Discussion ····· 4

Energy levels calculated by DFT ····· 4

Optical and electrochemical properties ····· 4

Single crystal data of the compounds ····· 6

Packing structure of rubrene ····· 7

Intermolecular electronic coupling versus extension of molecular π-backbone ····· 7

Characterization of the single crystals ····· 9

The transistor curves of the SC-OFETs in linear regime ····· 10

Theoretical mobilities of the materials in ideal crystals ····· 13

Thin-film OFETs ····· 15

References ····· 17

Author Contributions ····· 17

Experimental Procedures

Synthesis of compounds

The chemical reagents and solvents were directly used as received from commercial companies without further purification except additional notification. Compound **1** and **3** were prepared by following the literature reported procedure.[S1,S2]

Methyl thiohypochlorite (MeSCl) solution. To a 3-neck flask (50 mL) degassed with Argon (Ar), dichloromethane (DCM) (10 mL, anhydrous) was added, and the system was cooled down to 0 ˚C. Dimethyl sulfide (MeSSMe) (1.06 mL, 12.00 mmol) and sulfuryl chloride (SO_2Cl_2) (0.40 mL, 5.00 mmol) were added successively to the solution, and the mixture was stirred at 0 ˚C for 30 min. The as-prepared MeSCl solution was supposed to have the concentration of 1 M and the solution was directly used for the next step without further purification.

Compound **2**. To a 3-neck flask (100 mL) degassed with Ar, compound **1** (420 mg, 1.00 mmol) and DCM (30 mL, anhydrous) were added successively. The solution was cooled down to 0 ˚C, and the MeSCl solution (1 M, 3 mL) was added slowly to the solution. The resulting mixture was stirred at 0 ˚C for 1 h, and afterwards it was quenched by slow addition of H_2O (10 mL). The mixture was extracted with DCM, and the crude product was obtained by evaporating the solvent as light yellow powder (487 mg, quant.). ^{1}H NMR δ_H ($CDCl_3$, 400 MHz) 8.55 (4H, s, Ar-H), 2.41 (6H, s, $SCH_3 \times 2$), 0.50 (18H, s, $CH_3 \times 6$); MS (EI$^+$) *m/z* [M$^+$] found 476, formula $C_{22}H_{28}S_4Si_2$ [M$^+$] calc. 476.0612.

β-MT-NDT. In a single-neck flask (200 mL), compound **2** (715 mg, 1.50 mmol) was dissolved in tetrahydrofuran (THF, 30 mL). A tetrabutylammonium fluoride solution (TBAF, 1 M in THF, 30 mL) was added slowly to the resulted solution. The mixture was stirred for 4 h at room temperature (RT), and then the reaction was quenched by addition of H_2O (100 mL), which yielded precipitate. The crude product was obtained by filtration and washed with methanol (MeOH) to give light yellow powder (468 mg, 94%). ^{1}H NMR δ_H ($CDCl_3$, 400 MHz) 8.54 (2H, s, Ar-H), 8.43 (2H, s, Ar-H), 7.25 (2H, s, Ar-H), 2.62 (6H, s, $SCH_3 \times 2$); ^{13}C NMR δ_C (TCE-d_2, 100 MHz, 110 ˚C) 137.64, 137.58, 128.88, 128.78, 124.76, 121.52, 119.69, 17.11; HR-MS (EI$^+$) *m/z* [M$^+$] found 331.9836, formula $C_{16}H_{12}S_4$ [M$^+$] calc. 331.9822.

Compound **4**. Compound 4 was synthesized by the same procedure as the synthesis of compound **2**, with compound **3** (547 mg, 1.00 mmol), DCM (50 mL, anhydrous), and MeSCl solution (2 M, 5 mL). The crude product was obtained as red powder by column chromatography (silica gel, DCM: hexane = 1:10) (510 mg, 75%). ^{1}H NMR δ_H ($CDCl_3$, 400 MHz) 9.21 (2H, d, J = 0.9 Hz, Ar-H), 9.12 (2H, d, J = 0.9 Hz, Ar-H), 2.51 (6H, s, $SCH_3 \times 2$), 1.13~1.03 (30H, m, $CH_2CH_3 \times 6$); MS (EI$^+$) *m/z* [M$^+$] found 678, formula $C_{32}H_{40}S_4Cl_2Si_2$ [M$^+$] calc. 678.0928.

Compound **5**. To a 3-neck flask (300 mL) degassed with Ar, compound **4** (560 mg, 0.83 mmol), THF (60 mL, anhydrous) were added successively, and the solution was cooled down to 0 ˚C. Lithium aluminium hydride (LAH) (567 mg, 15 mmol) was added to the solution in small portions. The mixture was refluxed for 3 h, and then cooled down to 0 ˚C again. The reaction was quenched by H_2O (0.6 mL), aqueous sodium hydroxide (NaOH, 15% in H_2O, 0.6 mL), and H_2O (1.8 mL), successively. After that, H_2O (200 mL) was added to the mixture to get precipitate, which was collected by filtration and further treated with hydrochloric acid (HCl, 5 M, 100 mL). After filtration, the solid was obtained as the crude product, which was red powder and directly used for the next step without further purification (430 mg, 85%). ^{1}H NMR δ_H ($CDCl_3$, 400 MHz) 8.82 (2H, s, Ar-H), 8.70 (2H, s, Ar-H), 8.55 (2H, s, Ar-H), 2.47 (6H, s, $SCH_3 \times 2$), 1.10~1.05 (30H, m, $CH_2CH_3 \times 6$); MS (EI$^+$) *m/z* [M$^+$] found 610, formula $C_{32}H_{42}S_4Si_2$ [M$^+$] calc. 610.1708.

β-MT-ADT. To a 3-neck flask (300 mL) degassed with Ar, potassium hydroxide (KOH, 34 g, 606.06 mmol) was added, which was dissolved in MeOH (100 mL, anhydrous) and THF (40 mL, anhydrous). Compound **5** (430 mg, 0.70 mmol) was added to the solution, and the mixture was refluxed for 3 h. After that, the system was cooled down to 0 ˚C, and H_2O (200 mL) was added to precipitate. The solid was obtained as a crude product by filtration and successively washed with MeOH and diethyl ether to give red powder (202 mg, 76%). ^{1}H NMR δ_H (TCE-d_2, 400 MHz, 120 ˚C) 8.82 (2H, s, Ar-H), 8.63 (2H, s, Ar-H), 8.58 (2H, s, Ar-H), 7.35 (2H, s, Ar-H), 2.69 (6H, s, $SCH_3 \times 2$); ^{13}C NMR spectra could not be collected because of the low solubility of β-MT-ADT; HR-MS (EI$^+$) *m/z* [M$^+$] found 381.9978, formula $C_{20}H_{14}S_4$ [M$^+$] calc. 381.9978.

Methods and instruments

Nuclear magnetic resonance (NMR) spectra were obtained from a JEOL ECS 400 spectrometer operating at 400 MHz for ^{1}H or 100 MHz for ^{13}C with TMS as internal reference. Single-crystal X-ray analysis was carried out on a Rigaku R-AXIS RAPID (Cu*K*α radiation, λ = 1.541 Å, graphite monochromator). The structure was solved by direct methods. Non-hydrogen atoms were refined anisotropically, and hydrogen atoms were included in the calculations but not refined. All calculations were performed using the crystallographic software package CrystalStructures 4.2.[S3] UV-vis spectra were recorded on a Shimadzu UV-3600 spectrometer. Cyclic voltammograms (CVs) were recorded on a ALS Electrochemical Analyzer Model 612D in benzonitrile with tetrabutylammonium hexafluorophosphate (Bu_4NPF_6, 0.1 M) as the supporting electrolyte at a scanning rate of 100 mV/s. Pt was used as working and counter electrodes, and Ag/AgCl was used as the reference electrode. Ferrocene/ferrocenium redox couple (Fc/Fc$^+$) was used as external reference. The ionization potentials of the materials in the thin-film state were recorded by photoelectron spectroscopy in air from a RIKEN KEIKI AC-2 photoelectron spectrometer.

β-MT-NDT and β-MT-ADT were purified by the vacuum sublimation method twice before device fabrication. Organic field-effect transistors (OFETs), both single-crystal OFETs (SC-OFETs) and thin-film OFETs, were fabricated on octadecyltrichlorosilane (ODTS)-modified, heavily doped n$^+$-Si (100) wafer with 200 nm thermally grown SiO_2 (C_i = 17.3 nF cm^{-2}). Single crystals suitable for SC-OFETs were directly grown on the substrates through a physical vapor transport (PVT) method. On top of the single crystals, Au (50 nm) was deposited as the drain and source electrodes through a shadow mask with the channel length (*L*) of 40 µm. Thin films of β-MT-NDT with a thickness of 30 nm were vacuum-deposited on the substrates at the deposition rate of 0.8 Å s^{-1} under ~10^{-3} Pa pressure. Thin films of β-MT-ADT were prepared with the same method at the deposition rate of 0.5 Å s^{-1}. On top of the thin films, Au (50 nm) was deposited as drain and source electrodes through a shadow mask with *L* and channel width (*W*) of 50 µm and 1500 µm, respectively. The devices were characterized at room temperature under ambient

conditions with a Keithley 4200 semiconducting parameter analyzer. Field-effect mobilities (μ) was calculated in the saturation regime and linear regime using the following equations (1a) and (1b), respectively:

$$I_D = C_i\mu\left(\frac{W}{2L}\right)(V_G - V_{th})^2 \ (1a), \ \ I_D = C_i\mu V_D\left(\frac{W}{L}\right)(V_G - V_{th}) \ (1b)$$

where C_i is the capacitance of the SiO_2 insulator, V_D is the source-drain voltage, V_G and V_{th} are the gate and threshold voltages, respectively.

Thin-film X-Ray Diffractions (XRD) patterns were obtained with a Rigaku Ultima IV diffractometer with a Cu Kα source (λ = 1.541 Å) in air. Dynamic force-mode atomic force microscopic images were obtained with Nanocute scanning probe microscope system (SII Nanotechnology, Inc.) by using a canti-lever, SI-DF20 (Seiko Instruments Inc.). Theoretical calculations were carried out at the B3LYP/6-31G(d) level using Gaussian 09 program package.[S4] Calculations of the transfer integrals in different molecular dimers were performed with the Amsterdam density functional (ADF) program.[S5]

Results and Discussion

Energy levels calculated by DFT

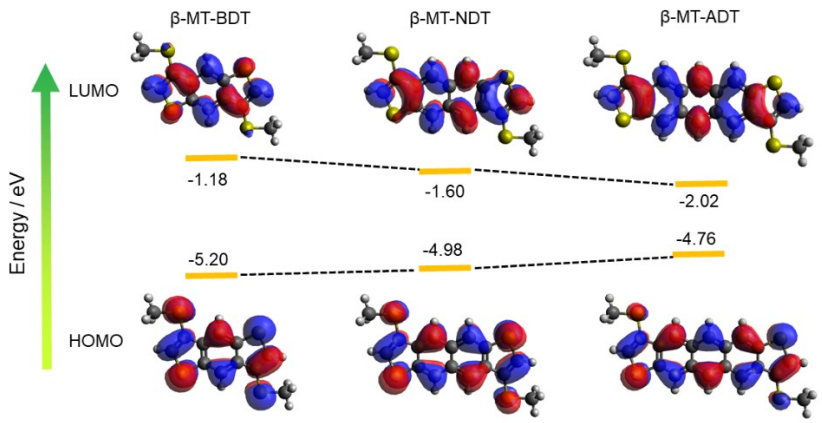

Figure S1. HOMO and LUMO energy levels of the β-MT-acenedithiophenes.

Figure S1 shows the distribution of HOMO and LUMO coefficients of β-MT-BDT, β-MT-NDT and β-MT-ADT, respectively. Similar to β-MT-BDT, the methylthio groups in β-MT-NDT and β-MT-ADT are in the same plane with the molecular backbone, and they have certain contribution to the HOMO coefficients as well. The HOMO energy levels are gradually increased from β-MT-BDT to β-MT-NDT, and further to β-MT-ADT, while the LUMO levels decrease, thus the bandgaps are narrowed. This trend of molecular energy level and bandgap change is corresponding to the π-expansion of the molecular core backbone.

Optical and electrochemical properties

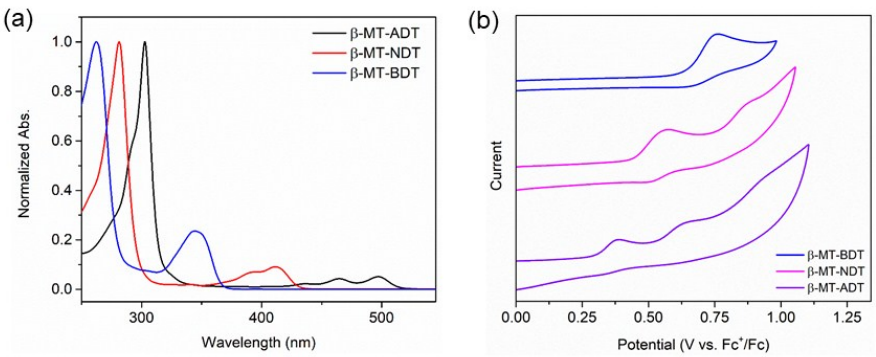

Figure S2. Optical and electrochemical properties of the compounds.

β-MT-BDT

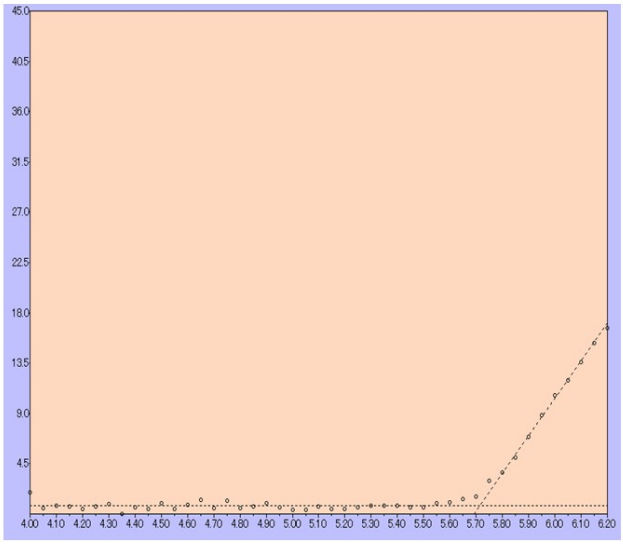

β-MT-NDT

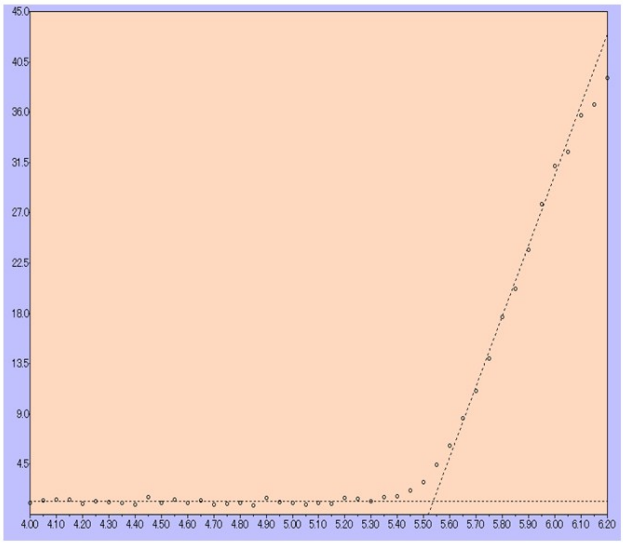

β-MT-ADT

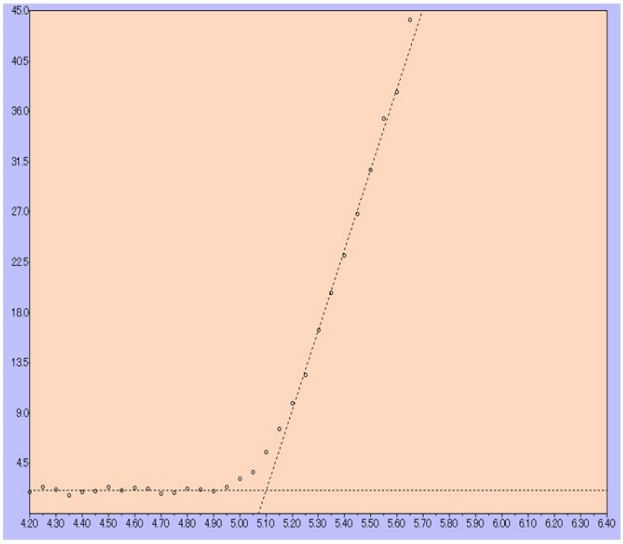

Figure S3. Photoelectron spectra of the thin films of the β-MT-acenedithiophenes.

Figure S2a shows the normalized UV-vis absorption spectra of β-MT-BDT, β-MT-NDT and β-MT-ADT in chloroform. The absorption edges (λ_{onset}s) of the three compounds shift from UV-region (365 nm for β-MT-BDT) to visible-region (430 nm for β-MT-NDT and 515 nm for β-MT-ADT), as the π-backbone is extended. Thus, consistent with the theoretical calculations, the optical bandgap of the molecules is decreased accordingly. As shown in the cyclic voltammetry (CV) curves (Figure S2b), with the increase of π-electrons, the molecules exhibit more and more complex oxidative behaviors, i.e., β-MT-BDT shows only one irreversible oxidative peak, while β-MT-NDT has two irreversible oxidative peaks, and β-MT-ADT owns three irreversible oxidative peaks. The onset of the first oxidative peak (E^{OX}_{onset}) relative to the Fc/Fc^+ external reference, is shifted from 0.65 V (β-MT-BDT) to 0.45 V (β-MT-NDT), and β-MT-ADT shows the lowest E^{OX}_{onset} (0.30 V). The HOMO energy levels of the molecules can be estimated as −5.45 eV for β-MT-BDT, −5.25 eV for β-MT-NDT and −5.10 V for β-MT-ADT, respectively. Table S1 summarized the energy levels of the frontier orbitals. The ionization potentials of these molecules in the thin-film state showed a similar trend with their HOMO energy levels determined by CV (Table S1). It is noteworthy that the IP of β-MT-ADT (5.1 eV) matches very well to the working function of gold (5.10 eV), suggesting that charge injection from the gold electrode to the organic semiconductor could be more efficient than the others.

Table S1. Summarized energy levels of the molecules.

Molecule	E^{OX}_{onset} (V)	HOMO (eV)	LUMO (eV)	E_g (eV)	IP (eV)
β-MT-BDT	0.65	−5.45	−2.05	3.40	5.71
β-MT-NDT	0.45	−5.25	−2.37	2.88	5.53
β-MT-ADT	0.30	−5.10	−2.69	2.41	5.10

Single crystal data of the compounds

Table S2. Summarized single crystal data of the compounds.

Compound	NDT	β-MT-NDT	β-MT-ADT
Formula	$C_{14}H_8S_2$	$C_{16}H_{12}S_4$	$C_{20}H_{14}S_4$
Molecular Weight	240.32	332.51	382.55
Crystal Habit	Platelet	Platelet	Block
Crystal System	triclinic	monoclinic	monoclinic
Space Group	*P*-1	$P2_1/c$	$P2_1/c$
a (Å)	5.8903 (3)	7.6311 (3)	7.45474 (15)
b (Å)	7.8065 (4)	17.4783 (7)	16.2651 (3)
c (Å)	11.6922 (6)	5.2771 (2)	6.76866 (16)
α (°)	90.453 (3)	-	-
β (°)	101.223 (3)	91.180 (3)	90.980 (2)
γ (°)	93.037 (3)	-	-
V (Å)^3	526.52 (4)	703.70 (5)	820.59 (3)
Temperature (K)	223	100	90
Z	2	2	2
R, R_w	0.0689, 0.2081	0.0754, 0.2144	0.0358, 0.0999
GOF	1.068	1.233	1.076

Packing structure of rubrene

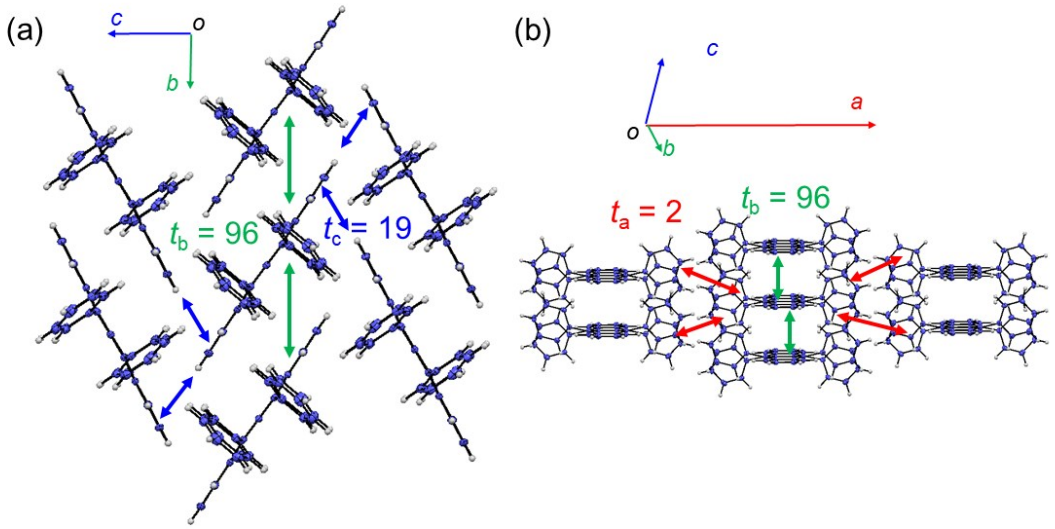

Figure S4. Packing structures of rubrene projected along (a) short- and (b) long-molecular axes. t_a, t_b and t_c (meV) are calculated values of intermolecular electronic coupling between HOMOs of neighboring molecules in each crystallographic axis direction.

Intermolecular electronic coupling versus extension of molecular π-backbone

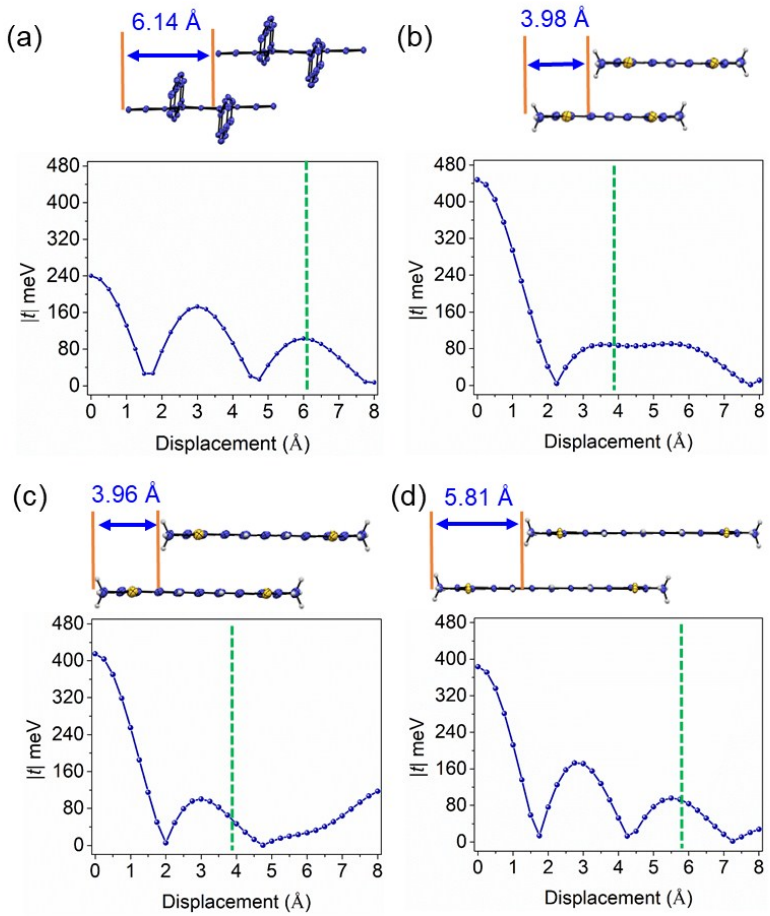

Figure S5. Transfer integral change vs. displacement of neighboring molecules in (a) rubrene, (b) β-MT-BDT, (c) β-MT-NDT, and (d) β-MT-ADT. The displacement direction of the molecules is slightly deflected from the long molecular axis, and in the calculation, the π-π distance is fixed at 3.5 Å for β-MT-acenedithiophenes.

To rationalize the effects of the molecular π-backbone to the intermolecular electronic couplings of neighboring molecules at specific mutual positions, *t* versus the displacement of the molecules in the π-stacking dimers (t_c) is calculated, since the π-stacking dimers afford the largest intermolecular orbital overlap in the pitched π-stacking.

As shown in Figure S5, the absolute values of *t* (without considering the phase effect) are plotted as a function of the displacement. In rubrene the 4 phenyl substituents are orthogonal to the molecular backbone, as a result, they do not contribute to the orbital overlap between neighboring molecules. Thus, only the molecular backbone (tetracene core) is included in the calculation. The actual displacement of 6.14 Å determined from crystal structure is located at the extrema in the displacement region of 4.5 Å to 7.5 Å, which is consistent with J. Brédas's report.[S6] In the plot of β-MT-BDT, there is a broad plateau with the displacement ranging from 3 Å to 7 Å. The actual displacement of 3.98 Å, determined from the crystal structure, is located in this plateau, yielding a large t_c. At this displacement, the methylthio groups in β-MT-BDT contribute significantly to its large t_c (Figure S6). However, β-MT-NDT with almost the same displacement of 3.96 Å is far from the extrema of t_c in the displacement ranging from 2 Å to 4 Å, suggesting that the actual displacement results in a disadvantageous mutual position for β-MT-NDT to achieve a large t_c. In sharp contrast, β-MT-ADT with a larger π-extension approaches an advantageous mutual position with t_c close to the extrema in the region of 4.5 Å to 7 Å, in spite of its large actual displacement of 5.81 Å.

It should be pointed out that the mutual position of β-MT-ADT is very similar to that of rubrene, in which the actual displacements are both located at the extrema. The advantageousness of this type of mutual position is reflected by not only the large *t* values achieved along the π-stacking direction, but also the possibility of lowering the dynamic disorder of the molecular crystals. In rubrene the orthogonal phenyl substituents hinder the sliding motion of neighboring molecules along the long molecular axis, and at the same time, the slight sliding motion does not change the *t* very much, because *t* is located at the extrema. This merit contributes the high mobilities of rubrene in SC-OFETs significantly based on the transient localization scenario.[S7, S8] On the other hand, in β-MT-ADT, along molecular edge the existence of the S-H and S-S intermolecular interactions (indicated by Hirshfeld surface analysis and SAPT0 calculation) can also hinder the long molecular axis sliding motion of neighboring molecules, which plays a similar role as that of the orthogonal phenyl substituents in rubrene. Since in β-MT-ADT the *t* is also located at the extrema, the dynamic disorder in β-MT-ADT crystals can also be lowered. This is another important reason that why β-MT-ADT achieves similar high performances in SC-OFETs as that of rubrene with SiO_2 as dielectric layer.

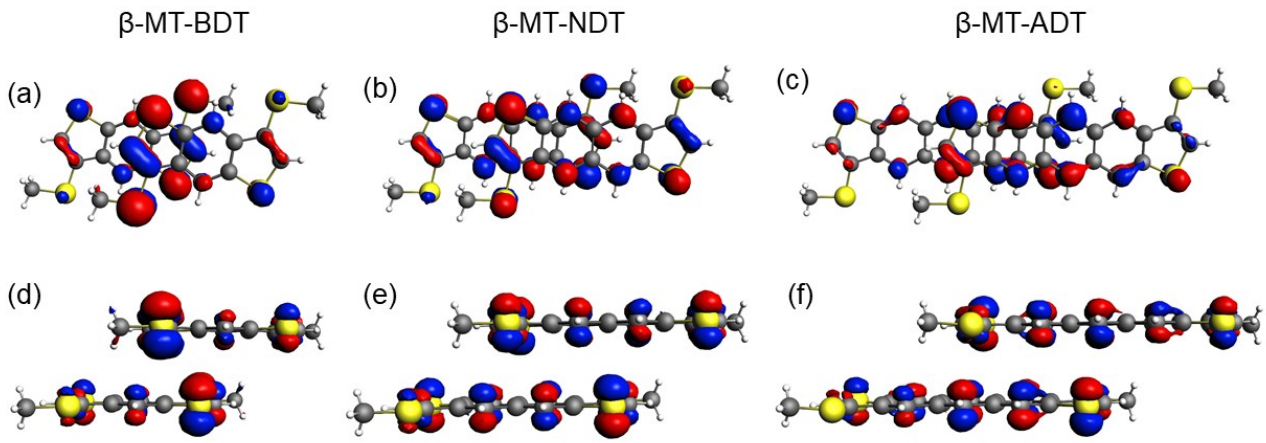

Figure S6. HOMOs (isosurface value: 0.03 au) for the dimmers in the π-stacking columns in the top-view ((a), (b), and (c)) and side-view ((d), (e), and (f)).

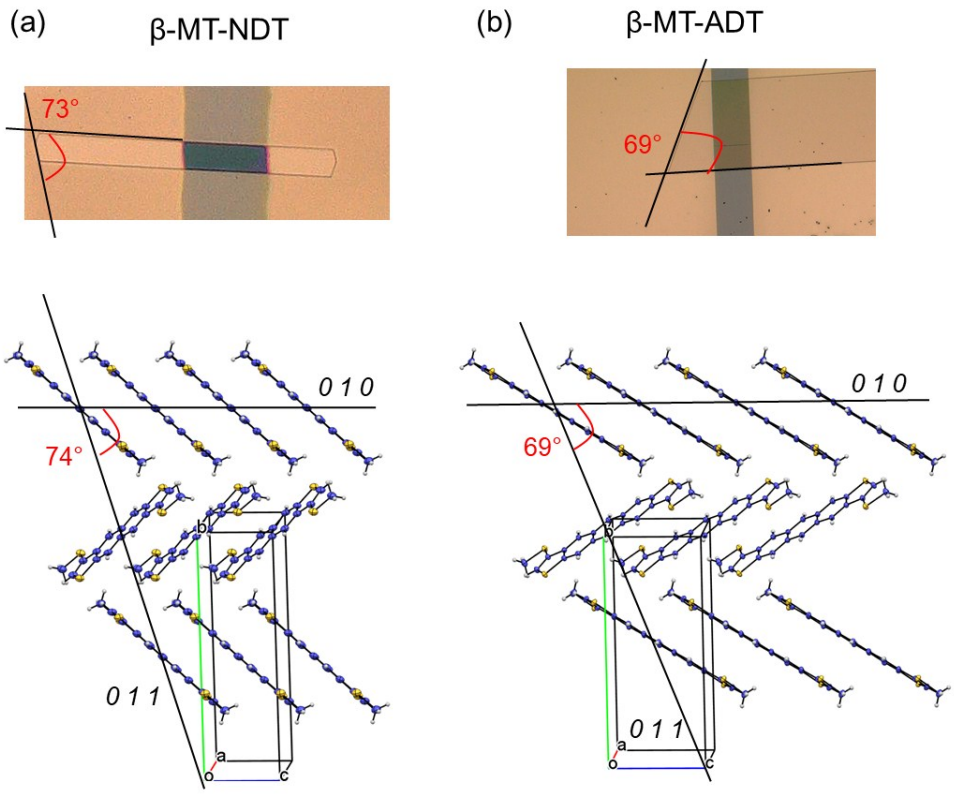

Characterization of the single crystals

Figure S7. Facet angels of the (a) β-MT-NDT and (b) β-MT-ADT crystals and the corresponding molecular packing patterns.

Figure S8. Out-of-plane XRD patterns of (a) β-MT-NDT and (b) β-MT-ADT single crystals on substrate (data collected at room temperature).

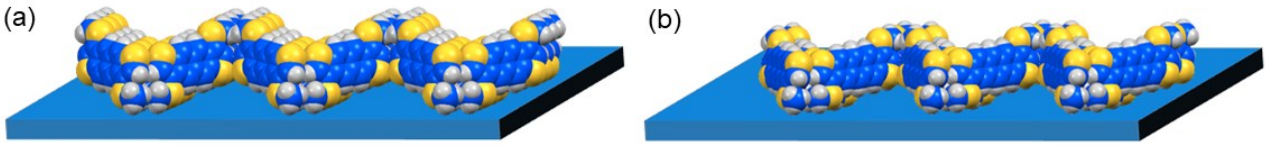

Figure S9. Schematic representation of the molecular orientation of (a) β-MT-NDT and (b) β-MT-ADT single crystals grown by PVT method on the substrate.

The transistor curves of the SC-OFETs in linear regime

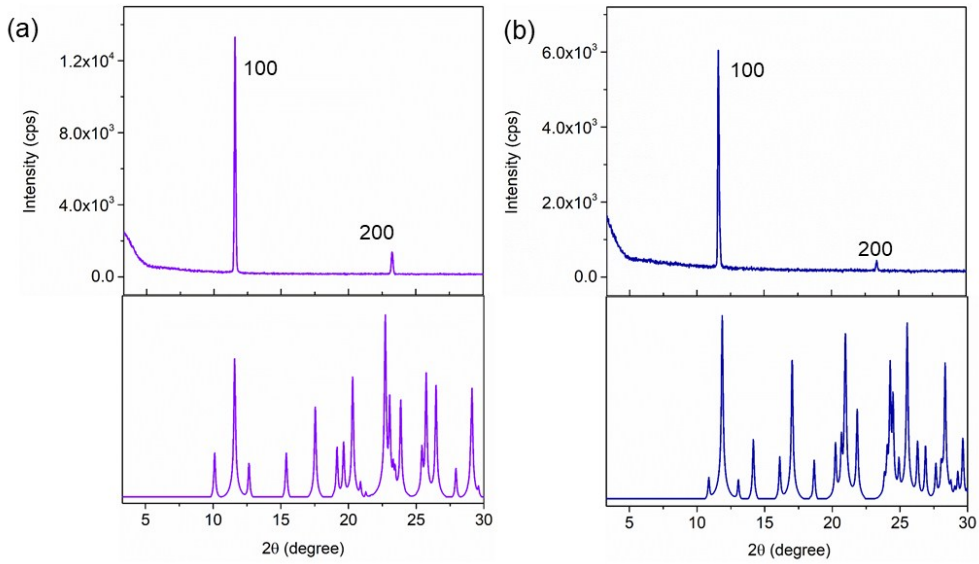

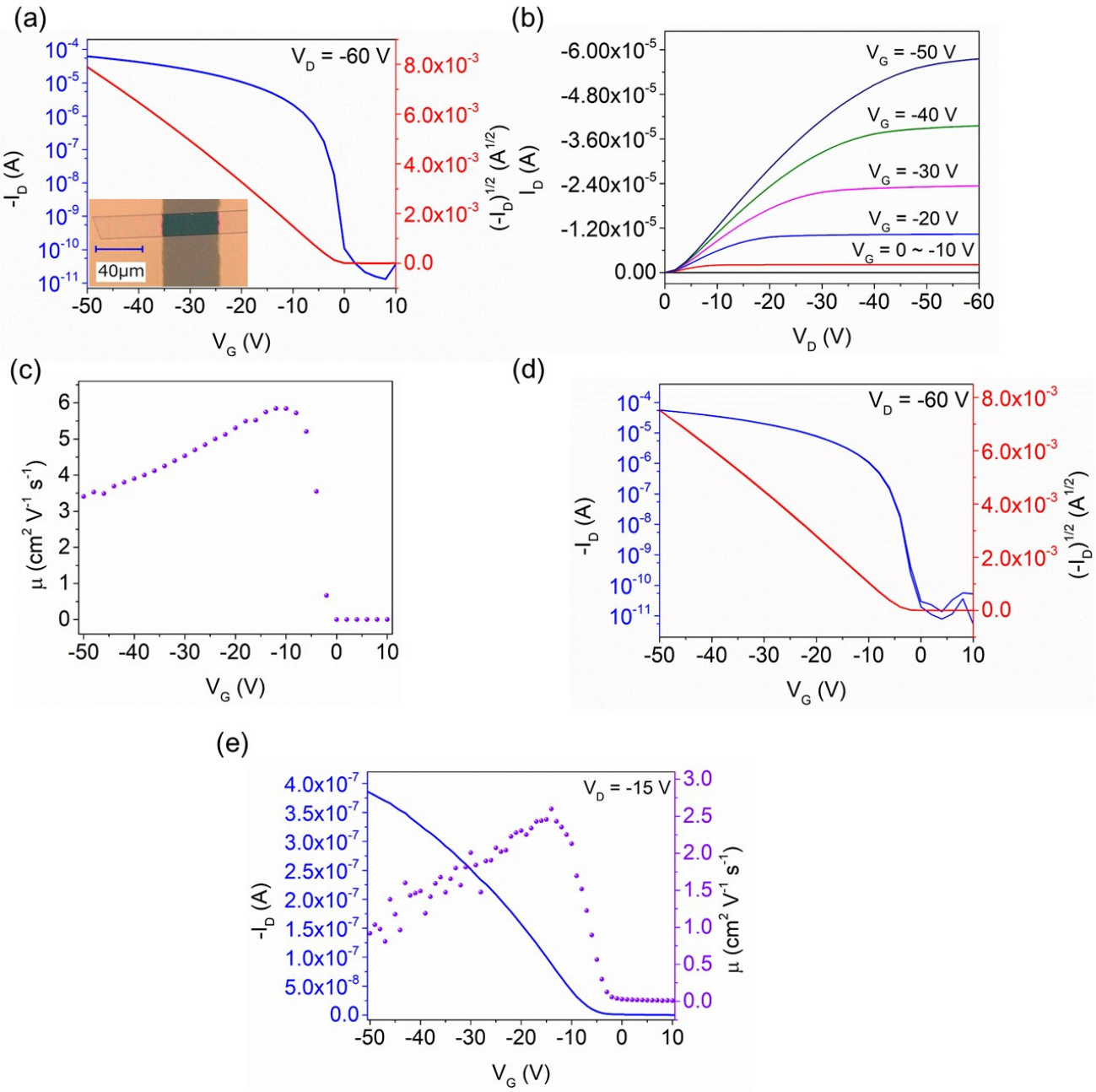

Figure S10. Transfer curves in saturation regime (a), output curves (b), gate-voltage dependent mobilities (c), hysteresis curves (d) and transfer curves in linear regime (e) of the rubrene based SC-OFETs. The device showed mobilities of 1.91 $cm^2 V^{-1} s^{-1}$ (ave., max of 2.32 $cm^2 V^{-1} s^{-1}$) in linear regime, which are reasonably agreed with the mobilities in saturation regime.

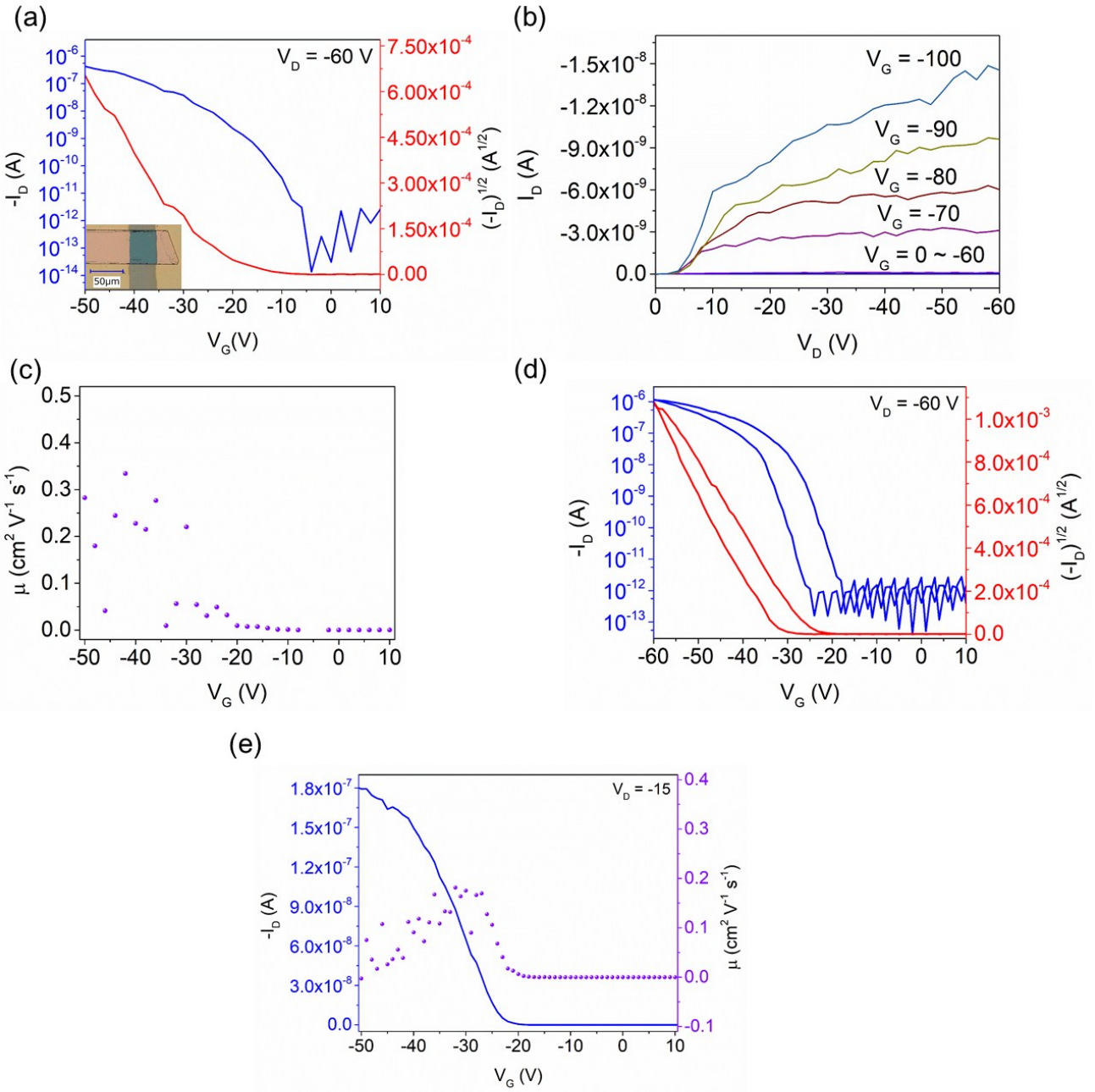

Figure S11. Transfer curves in saturation regime (a), output curves (b), and gate-voltage dependent mobilities of β-MT-BDT based SC-OFETs as reported in previous work (*Chem. Commun.*, 2017, 53, 9594-9597). Hysteresis curves (d) and transfer curves in linear regime (e) of the SC-OFETs. The device showed mobilities of 0.14 $cm^2 V^{-1} s^{-1}$ (ave., max of 0.21 $cm^2 V^{-1} s^{-1}$) in linear regime, which are reasonably agreed with the mobilities in saturation regime.

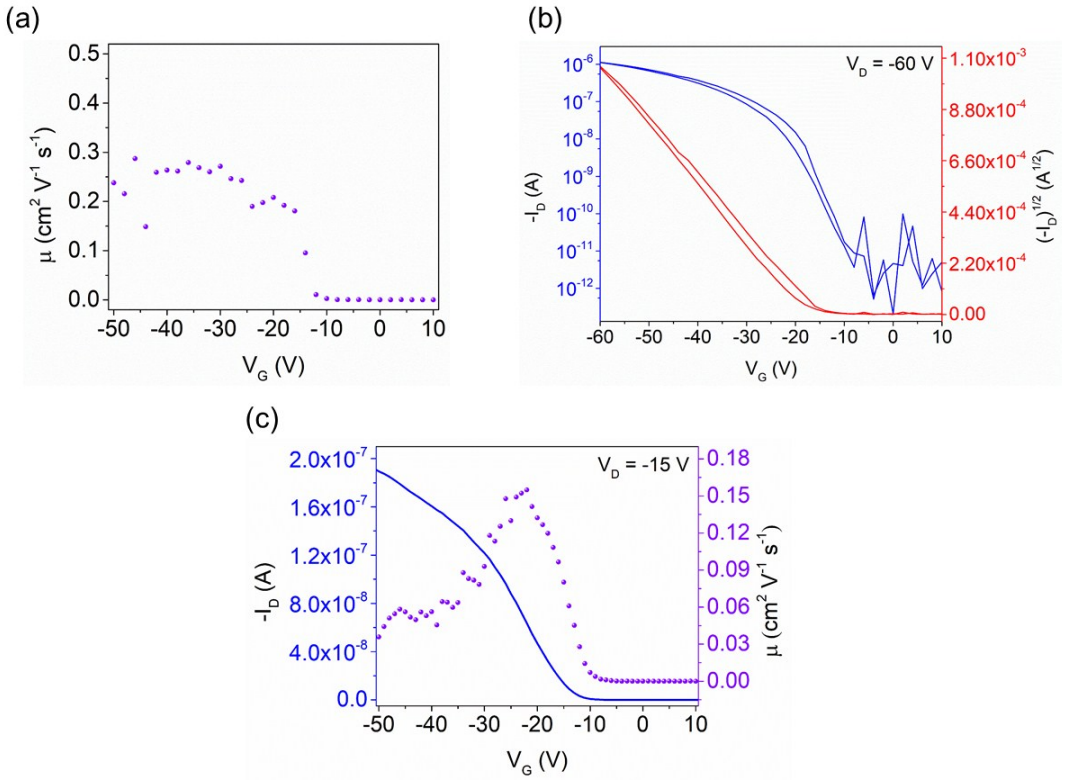

Figure S12. Gate-voltage dependent mobilities (a), hysteresis curves (b) and the transfer curves in linear regime (c) of the β-MT-NDT based SC-OFETs. The device showed mobilities of 0.12 $cm^2 V^{-1} s^{-1}$ (ave., max of 0.21 $cm^2 V^{-1} s^{-1}$) in linear regime, which are reasonably agreed with the mobilities in saturation regime.

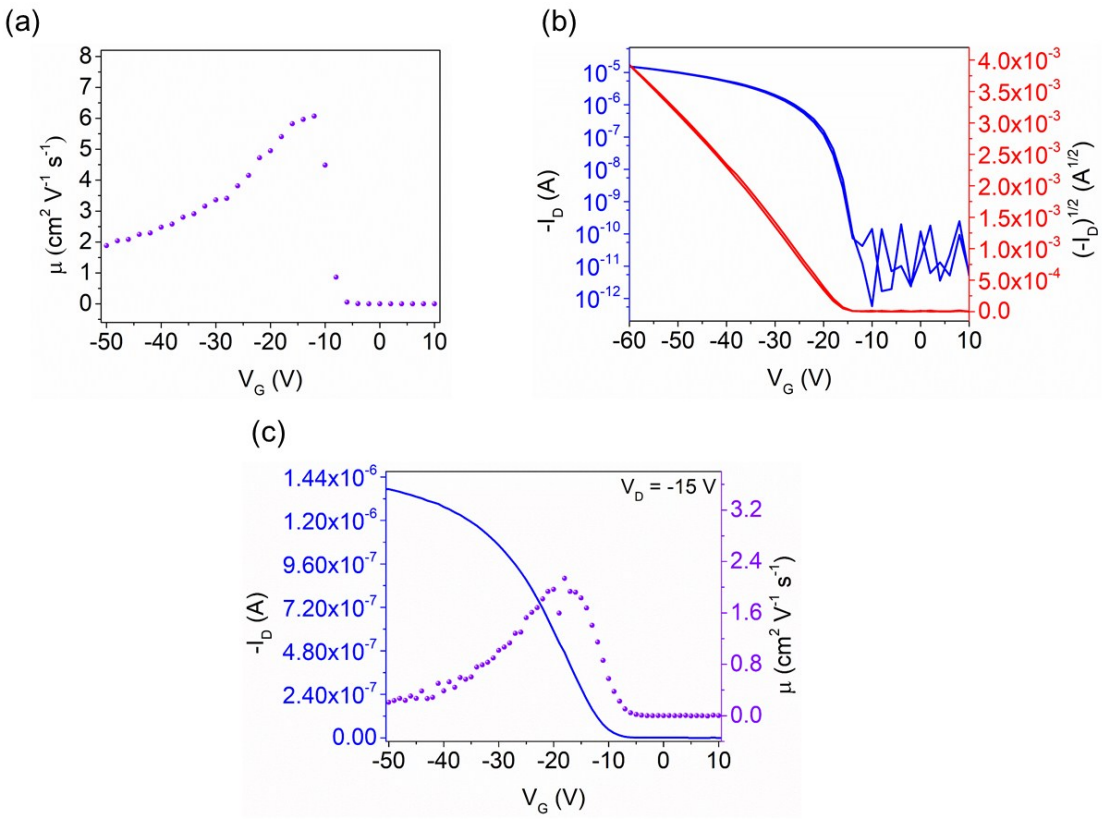

Figure S13. Gate-voltage dependent mobilities (a), hysteresis curves (b) and the transfer curves in linear regime (c) of the β-MT-ADT based SC-OFETs. The device showed mobilities of 1.86 $cm^2 V^{-1} s^{-1}$ (ave., max of 2.21 $cm^2 V^{-1} s^{-1}$) in linear regime, which are reasonably agreed with the mobilities in saturation regime.

Table S3. Averaged reliability factor of the SC-OFETs.

Materials	β-MT-BDT[a]	β-MT-NDT	β-MT-ADT	Rubrene
Average reliability factor (%)	39	51	61	72

Theoretical mobilities of the materials in ideal crystals

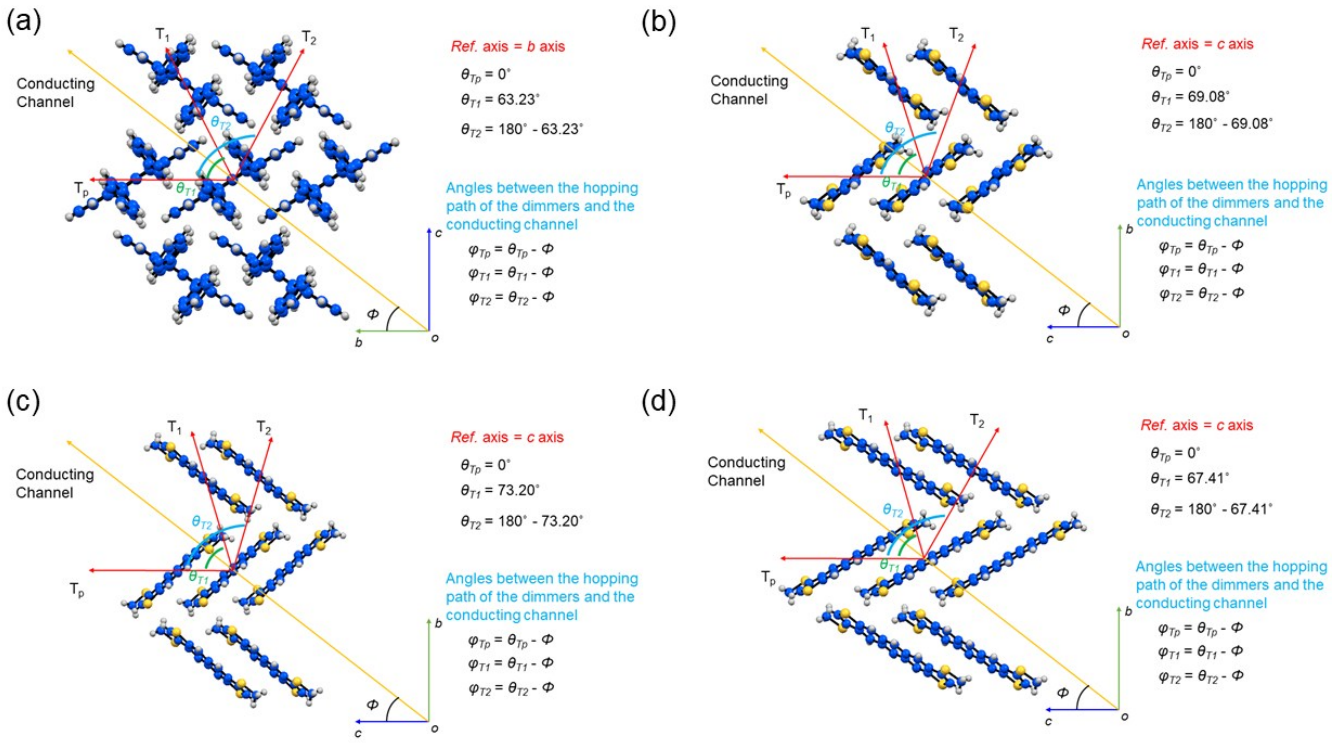

Figure S14. Illustration of projecting different hopping paths to a specific conducting channel in the molecular layers (a) rubrene, (b) β-MT-BDT, (c) β-MT-NDT and (d) β-MT-ADT.

β-MT-acenedithiophenes and rubrene form lamellar structures in the crystals and adopt the "edge-on" orientation on the substrate. The charge carrier transport can be regarded as a 2D transport behavior within the basal stacked molecular layers, which is along the *b*-*c* plane as judged from the crystal structures of β-MT-acenedithiophenes and rubrene. Within the molecular layer along a specific conducting direction, carrier transport can be determined by combining the electronic couplings from all the hopping pathways. The anisotropic mobility of the materials was calculated on the basis of the semi-classical Marcus theory with the parallel dimer hopping pathway as the reference axis.

In the conducting layer of β-MT-acenedithiophenes and rubrene, there are three types of hopping dimers, T_p (parallel dimers), T_1 and T_2 (transverse dimers), (red arrows in Figure S14). The reference axis is along the T_p hopping path, and the angles (θ) between the hopping paths (T_p, T_1 and T_2) to the reference axis are extracted from the crystal structure. To a specific conducting channel (orange arrows in Figure S14), with an angle (ϕ) to the reference axis, the angle between each hopping path and the conducting channel can be calculated as (φ). Thus, the projection of the transfer integrals to the conducting channel from each hopping path can be calculated from φ, which gives the combined hopping along the conducting channel, and the anisotropic mobilities referring to the reference axis can be calculated.[S11]

The electronic hopping rate (k_{ET}) is given by the Marcus-Hush equation (2):

$$k_{ET} = \frac{4\pi^2}{h}\frac{1}{\sqrt{4\pi\lambda k_B T}}t^2\exp\left(-\frac{\lambda}{4k_B T}\right) \qquad (2)$$

where λ is the reorganization energy, t is the transfer integral, and T is the temperature (300 K in this calculation); h and k_B is the Planck and Boltzmann constant, respectively.

The λ of the molecules was calculated by using the adiabatic potential energy surface method in equation (3):

$$\lambda = \lambda_0 + \lambda_+ = \left(E_0^* - E_0\right) + \left(E_+^* - E_+\right) \qquad (3)$$

where E_o^*, E_o, E_+^*, E_+, represent the energies of neutral in cationic geometry, neutral in neutral geometry, cation in neutral geometry, and cation in cationic geometry, respectively. For details, refer to the literature.[S10] The geometries for the isolated molecules in the neutral and cationic states were optimized using the B3LYP/6-31G(d) and (U)B3LYP/6-31G(d) level, respectively, with Gaussian 09 program package.
The hopping probability regarding to each hopping path can be calculated as by equation (4):

$$P_i = \frac{k_{ETi}}{\sum_i k_{ETi}} \qquad (4)$$

where *i* represents a specific hopping pathway.
Considering in this calculation the charge carrier mobility is calculated along a specific direction, thus the charge carrier transport is a one dimentional behavior. The diffusion coefficient D of the charge carriers can be calculated by equation (5):

$$D = \frac{\sum_i k_{ETi} r_i^2 P_i}{2} \qquad (5)$$

where r_i represents the hopping distance (the distance between the centroids of the dimers).
The drift mobility of charge carriers was derived from the Einstein relation shown in equation (6):

$$\mu = \frac{e}{k_B T} D \qquad (6)$$

where *e* is the electronic charge.
The projection of all the hopping paths leads to the charge carrier mobility (μ_ϕ) along a specific conducting channel as:

$$\mu_\phi = \frac{e}{2k_B T} \sum_i k_{ETi} r_i^2 P_i \cos^2(\theta_i - \phi) \qquad (7)$$

For rubrene, μ_ϕ is as:

$$\mu_\phi = 0.015\cos^2(63.23 - \phi) + 0.015\cos^2(63.23 + \phi) + 7.67\cos^2(\phi) \qquad (8)$$

For β-MT-BDT, μ_ϕ is as:

$$\mu_\phi = 0.0057\cos^2(69.08 - \phi) + 0.0057\cos^2(69.08 + \phi) + 2.81\cos^2(\phi) \qquad (9)$$

For β-MT-NDT, μ_ϕ is as:

$$\mu_\phi = 0.0077\cos^2(73.20 - \phi) + 0.0077\cos^2(73.20 + \phi) + 1.62\cos^2(\phi) \qquad (10)$$

For β-MT-ADT, μ_ϕ is as:

$$\mu_\phi = 0.38\cos^2(67.41 - \phi) + 0.38\cos^2(67.41 + \phi) + 12.27\cos^2(\phi) \qquad (11)$$

Table S4. Summary of calculated reorganization energies and anisotropic mobilities.

compound	λ (meV)	t_c (meV)	t_b (meV)	μ ($cm^2 V^{-1} s^{-1}$)
β-MT-BDT	160	78	14	0.010 – 2.81
β-MT-NDT	116	45	9	0.014 – 1.62
β-MT-ADT	95	90	33	0.65 – 12.38
rubrene	159	96	19	0.024 – 7.68

As summarized in Table S4, β-MT-BDT has a moderately large λ (160 meV), and as the π-backbone of β-MT-acenedithiophenes increases, λ decreases to 116 meV for β-MT-NDT and 95 meV for β-MT-ADT. This is remarkably different from the rubrene case; λ of rubrene is reported to be 159 meV, which is close to that of β-MT-BDT and much larger than those of β-MT-NDT and β-MT-ADT.
The β-MT-acenedithiophenes show anisotropic charge carrier transporting behavior similar to that of rubrene, and the most efficient conductive direction is along the π-stacking, i.e., the crystallographic *c*-axis direction (Figure S14). The theoretical mobilities in β-MT-BDT crystals are in the range of 0.010 to 2.81 $cm^2 V^{-1} s^{-1}$. Although the largest *t* in β-MT-BDT is as large as 78 meV (i.e., t_c), the relatively large λ

limits the charge carrier mobility in the solid state. The λ of β-MT-NDT is much smaller than that of β-MT-BDT, but the smaller intermolecular electronic coupling (t_c = 45 meV) yields lower theoretical mobilities (0.014−1.62 cm^2 V^{-1} s^{-1}). β-MT-ADT shows the highest mobilities (0.65−12.38 cm^2 V^{-1} s^{-1}) among the β-MT-acenedithiophenes, reflecting the fact that the compound has both the largest t and the smallest λ among the series. The theoretical mobility of rubrene is calculated to be 0.024−7.68 cm^2 V^{-1} s^{-1}, which can be understood as an outcome of its larger t and λ than those of β-MT-ADT. The empirical mobilities have the same trend as the theoretical ones, and the former are slightly lower by severalfold than the latter, indicating that the present SC-OFETs are mostly of good quality.

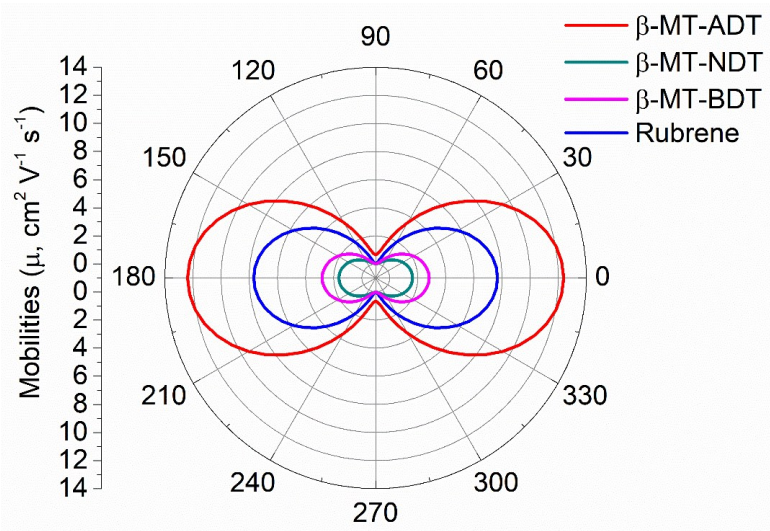

Figure S15. Calculated anisotropic mobilities of the molecules in ideal crystals (the 0° and 180° directions are along the π-stacking direction (crystallographic *c*-axis for the β-MT-acenedithiophenes and *b*-axis for rubrene (Figure S14)).

Thin-film OFETs

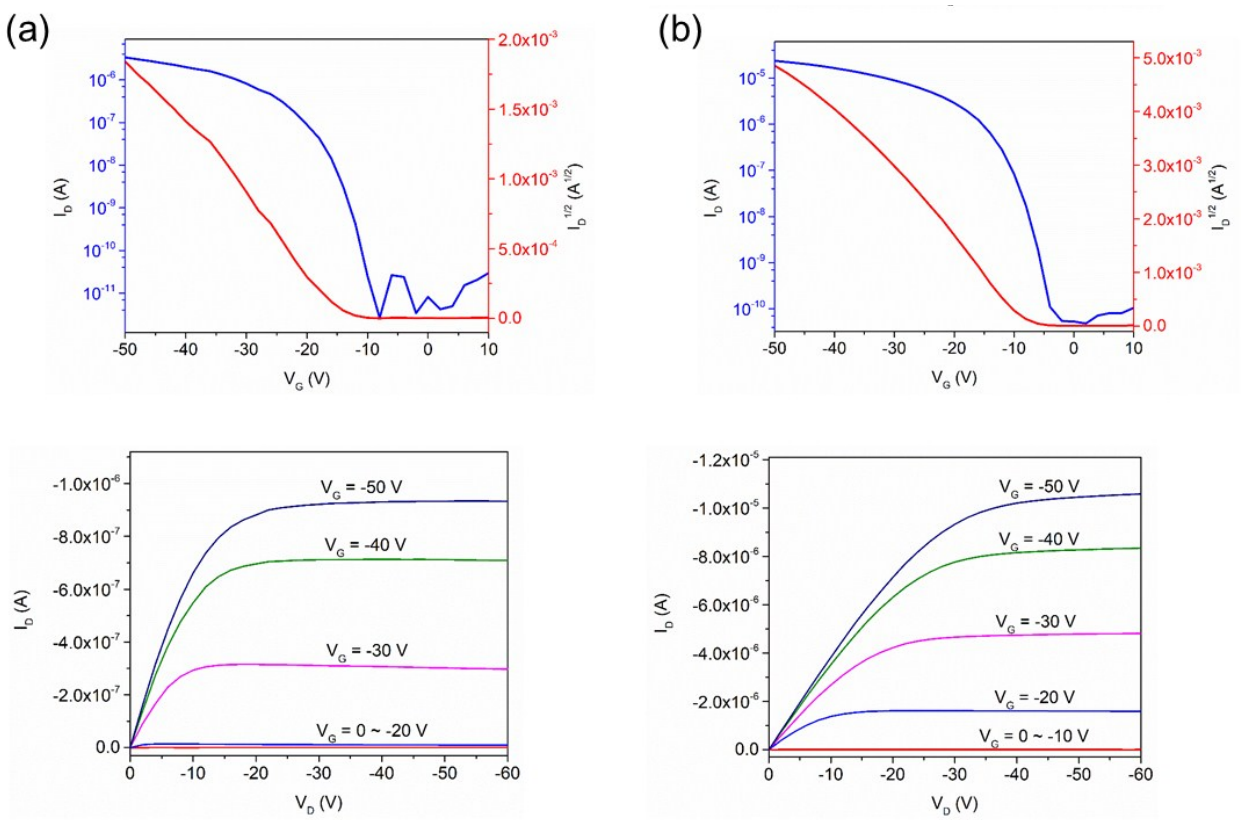

Figure S16. Transfer (up, (V_D = -60 V)) & output (down) curves of the thin-film OFETs (a) β-MT-NDT, (b) β-MT-ADT.

The thin films of β-MT-BDT consists of isolated crystalline grains, and because of this discontinuous thin-film nature, no thin-film OFETs were fabricated. Thin-film OFETs of β-MT-NDT showed average mobilities ca. 0.011 $cm^2 V^{-1} s^{-1}$ (Figure S16). The crystallinity of the thin films was confirmed by the two peaks in the out-of-plane X-ray diffraction (XRD) patterns, which could be assigned to 100 and 200 (Figure S17). From the AFM image of the thin films large crystalline grains (ca. 0.5 × 0.1 μm) were observed, and the surface of the thin film is very rough with roughness up to RMS ca. 16.6 nm (Figure S18). The average mobilities of β-MT-ADT based thin-film OFETs are ca. 0.047 $cm^2 V^{-1} s^{-1}$ (Figure S16), which is around 4 times higher than that of β-MT-NDT. The diffraction peak assigned to 100 in the XRD pattern suggests that the thin films are crystalline (Figure S17), which was also indicated by the AFM image, showing clear crystalline grains (Figure S18). Note that as same as in the single crystals, both β-MT-NDT and β-MT-ADT adopted "edge-on" molecular orientation in the thin film, determined by the XRD patterns. Even though the size of the crystalline grains in β-MT-ADT thin films is quite small (ca. 0.05 × 0.1 μm), the surface is still very rough (RMS ca. 16.2 nm). Table S4 summarizes the detailed parameters of the thin-film OFETs based on the molecules.

Table S5. Summarized parameters of the thin-film OFETs based on the molecules

Molecules	β-MT-BDT[a]	β-MT-NDT	β-MT-ADT	Rubrene[b]
Mobility ($cm^2 V^{-1} s^{-1}$)	--- (---)	0.011 (0.018)	0.047 (0.052)	~10^{-5}
V_{th} (V)	---	−14.0	−7.3	---
ON/OFF ratio	---	10^5 – 10^6	10^4 – 10^5	---

[a] The thin-film OFETs cannot be fabricated because of the discontinuous nature of the thin films. [b] The reported mobility is from a bottom-gate/bottom-contact device configuration on Si/SiO_2 substrate from ref. S9; the V_{th} and ON/OFF ratio were not reported.

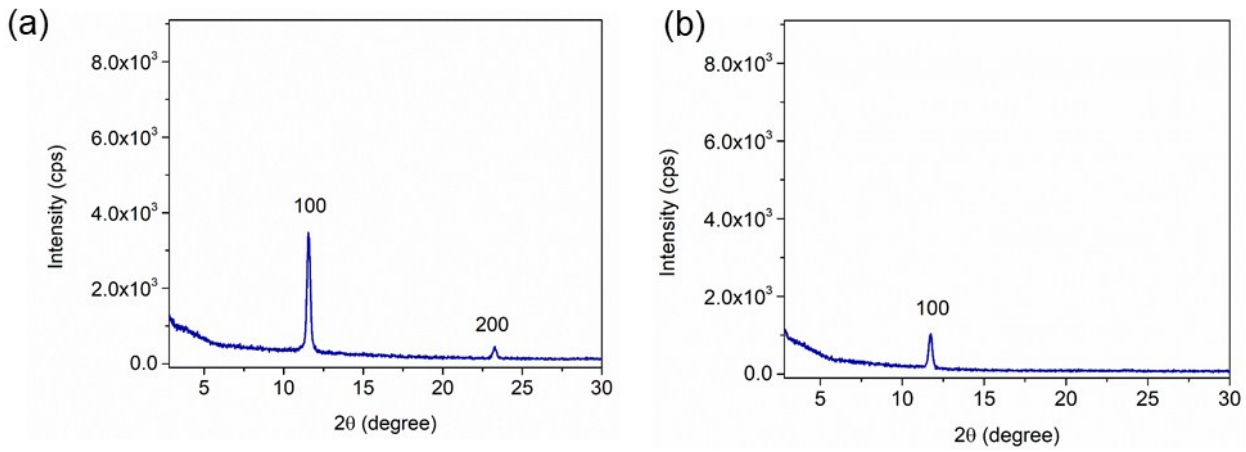

Figure S17. Out-of-plane XRD patterns of (a) β-MT-NDT and (b) β-MT-ADT thin films.

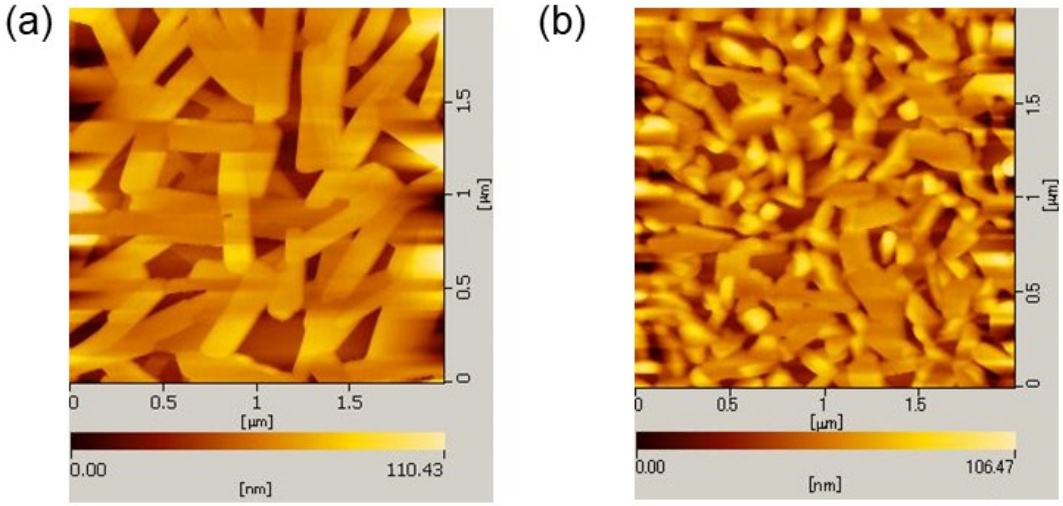

Figure S18. AFM images of (a) β-MT-NDT and (b) β-MT-ADT thin film.

References

S1 Shinamura, S. *et al.* Linear- and Angular-Shaped Naphthodithiophenes: Selective Synthesis, Properties, and Application to Organic Field-Effect Transistors. *J. Am. Chem. Soc.* **133**, 5024-5035, (2011).

S2 Nakano, M. *et al.* Isomerically Pure Anthra[2,3-b:6,7-b']-difuran (anti-ADF), -dithiophene (anti-ADT), and -diselenophene (anti-ADS): Selective Synthesis, Electronic Structures, and Application to Organic Field-Effect Transistors. *J. Org. Chem.* **77**, 8099-8111, (2012).

S3 Rigaku Cooperation crystal structure analysis package, https://www.rigaku.com/ja/products/protein/cs.

S4 Gaussian 09, Revision D.01, Frisch, M. J.; Trucks, G. W.; Schlegel, H. B.; Scuseria, G. E.; Robb, M. A.; Cheeseman, J. R.; Scalmani, G.; Barone, V.; Mennucci, B.; Petersson, G. A.; Nakatsuji, H.; Caricato, M.; Li, X.; Hratchian, H. P.; Izmaylov, A. F.; Bloino, J.; Zheng, G.; Sonnenberg, J. L.; Hada, M.; Ehara, M.; Toyota, K.; Fukuda, R.; Hasegawa, J.; Ishida, M.; Nakajima, T.; Honda, Y.; Kitao, O.; Nakai, H.; Vreven, T.; Montgomery, J. A., Jr.; Peralta, J. E.; Ogliaro, F.; Bearpark, M.; Heyd, J. J.; Brothers, E.; Kudin, K. N.; Staroverov, V. N.; Kobayashi, R.; Normand, J.; Raghavachari, K.; Rendell, A.; Burant, J. C.; Iyengar, S. S.; Tomasi, J.; Cossi, M.; Rega, N.; Millam, J. M.; Klene, M.; Knox, J. E.; Cross, J. B.; Bakken, V.; Adamo, C.; Jaramillo, J.; Gomperts, R.; Stratmann, R. E.; Yazyev, O.; Austin, A. J.; Cammi, R.; Pomelli, C.; Ochterski, J. W.; Martin, R. L.; Morokuma, K.; Zakrzewski, V. G.; Voth, G. A.; Salvador, P.; Dannenberg, J. J.; Dapprich, S.; Daniels, A. D.; Farkas, Ö.; Foresman, J. B.; Ortiz, J. V.; Cioslowski, J.; Fox, D. J. Gaussian, Inc., Wallingford CT, 2009.

S5 ADF: powerful DFT code for modeling molecules; Scientific Computing and Modeling: Amsterdam; http://www.scm.com/ADF/.

S6 da Silva Filho, D. A., Kim, E. G. & Brédas, J. L. Transport Properties in the Rubrene Crystal: Electronic Coupling and Vibrational Reorganization Energy. *Adv. Mater.* **17**, (2005).

S7 Fratini, S., Ciuchi, S., Mayou, D., de Laissardière, G. T. & Troisi, A. A map of high-mobility molecular semiconductors. *Nat. Mater.* **16**, 998, (2017)

S8 Fratini, S., Mayou, D. & Ciuchi, S. The Transient Localization Scenario for Charge Transport in Crystalline Organic Materials. *Adv. Funct. Mater.* **26**, 2292-2315, (2016).

S9 Wen, S.-H. *et al.* First-Principles Investigation of Anistropic Hole Mobilities in Organic Semiconductors. *J. Phys. Chem. B* **113**, 8813-8819, (2009).

S10 Hutchison, G. R., *et al.* Hopping Transport in Conductive Heterocyclic Oligomers: Reorganization Energies and Substituent Effects. *J. Am. Chem. Soc.* **127**, 2339-2350, (2005).

S11 Seo, S. *et al.* Ambipolar Rubrene Thin Film Transistors. *Appl. Phys. Lett.* **88**, 232114, (2006).

Author Contributions

C.W. and K.T. designed the project. C.W. performed the experiments and analyzed the data. D.H. analyzed the single crystal of β-MT-ADT. M.N., H.T., and K.K. helped in the synthesis of the materials. T.O. assisted in the SAPT calculation. C.W. and K.T. wrote the manuscript.